Published in final edited form as:
J Magn Reson Imaging. 2012 October ; 36(4): 933–942. doi:10.1002/jmri.23714.

High Temporal and Spatial Resolution Imaging of Peripheral Vascular Malformations

Petrice M. Mostardi, BS, **Phillip M. Young, MD**, **Michael A. McKusick, MD**, and **Stephen J. Riederer, PhD***
Department of Radiology, Mayo Clinic, Rochester, Minnesota, USA.

Abstract

Purpose—To assess the performance of a recently developed 3D time-resolved CE-MRA technique, Cartesian Acquisition with Projection-Reconstruction-like sampling (CAPR), for accurate characterization and treatment planning of vascular malformations of the periphery.

Materials and Methods—Twelve patient studies were performed (eight female, four male; average age, 33 years). The protocol consisted of three-dimensional (3D) time-resolved CE-MRA followed by a single late phase T1-weighted acquisition. Vascular malformations were imaged in the forearm, hand, thigh, and foot. Imaging evaluation was performed for accurate characterization of lesion type, identification of feeding and draining vessels, involvement with surrounding tissue, overall quality for diagnosis and treatment planning, and correlation with conventional angiography.

Results—Time-resolved CE-MRA allowed for characterization of malformation flow and type. Feeding and draining vessels were identified in all cases. Overall quality for diagnosis and treatment planning was 3.58/4.0, and correlation with conventional angiography was scored as 3.89/4.0.

Conclusion—The CAPR time series has been shown to portray the temporal dynamics and structure of vascular malformations as well as the normal vasculature with high quality. CAPR time-resolved imaging is able to accurately characterize high and low flow lesions, allowing for pretreatment lesion assessment and treatment planning. Delayed imaging is important to capture complete filling of very slow flow vascular malformations.

Keywords

CE-MRA; time-resolved imaging; peripheral vascular malformations

VASCULAR MALFORMATIONS ARE defects in the circulatory system generally formed during development. They are present in approximately 1.5% of the population and may lead to pain, pathologic bone fractures, and muscle contractures as a result of invasion into surrounding tissue structures (1). Treatment of vascular malformations is targeted at destruction of the nidus, reduction of potential for growth of the vascular malformation, and prevention of clinical consequences. However, treatment options are relatively limited and may worsen symptoms if not appropriately applied (2). Treatment planning requires accurate characterization of the vascular lesion including: (i) the extent of the vascular

* Address reprint requests to: Department of Radiology, Mayo Clinic, Opus 2-133, 200 First Street SW, Rochester, MN 55905. riederer@mayo.edu.

Additional Supporting information may be found in the online version of this article. The Supplementary Material referred to in this article can be found at http://www.interscience.wiley.com/jpages/1058-8388/suppmat

malformation (focal, multifocal, or diffuse), (ii) its involvement with surrounding tissue (muscle, bone, nerves, tendons, subcutaneous tissue, and skin), (iii) the feeding and draining vessels, and (iv) the classification of the lesion. Vascular malformations are most commonly classified by flow rate (high flow versus low flow) (3) and type (arterial, venous, capillary, lymphatic, or mixed) (4). Low flow lesions are generally treated with sclerotherapy, which involves direct injection of a sclerosing agent to the nidus of the vascular malformation. Treatment of high flow lesions generally requires a multifaceted approach, and sclerotherapy with flow control by means of embolization is often used as one part of treatment (2).

Characterization of vascular malformations is generally done with imaging techniques such as digital subtraction angiography (DSA), ultrasound (US), and more recently, MRI. DSA provides high temporal (≤ 1 s frame time) and high spatial resolution (≤ 1 mm) but is an invasive procedure that uses iodinated contrast material and ionizing radiation with images acquired as projections (5). Ultrasound may be used to image the flow of superficial lesions but lacks tissue penetration, has a small imaging field-of-view, and the exam quality is highly operator dependent. An MRI protocol using T1 and T2-weighted imaging is currently the preferred method as it offers noninvasive imaging with high spatial resolution that is able to characterize the structure of the lesion and its involvement with the surrounding tissue (6–10). MR angiography (MRA) (11–13) may be useful as part of the MR evaluation of vascular malformations (8). In particular, time-resolved contrast-enhanced MR angiography (CE-MRA) techniques (14,15) with both high temporal and spatial resolution may provide structural detail of the malformation and normal vasculature as well as functional information about the feeding and draining vessels and vascular malformation (3,16–18).

Time-resolved CE-MRA with short frame times and high spatial resolution has been made possible by the development of parallel acquisition. If applied along the two phase encoding directions of three-dimensional (3D) acquisition (19), parallel acquisition can provide acceleration factors (R) of 6 or higher (20,21). These can be combined with various ***k***-space sampling patterns (15,20,22), often in conjunction with view-sharing (23), to reconstruct image frames at a rate faster than that of the inherent acquisition time. When the acceleration (R) of 2D methods such as SENSE (19) is combined with the acceleration R_{HD} allowed by homodyne reconstruction, the overall net acceleration $R_{NET} = R \times R_{HD}$, can routinely be 10-fold or higher, making it possible to acquire time-resolved contrast-enhanced angiograms of the peripheral vasculature with 1-mm isotropic spatial resolution and ≤ 6-s frame time (24–26).

The purpose of this work is to assess the performance of a recently developed highly accelerated ($R_{NET} = 14.4$) 3D time-resolved CE-MRA technique, Cartesian Acquisition with Projection-Reconstruction-like sampling (CAPR), for accurate characterization and treatment planning of vascular malformations of the periphery.

MATERIALS AND METHODS

Patients

All studies were approved by the institutional review board and were Health Insurance Portability and Accountability Act compliant; written consent was obtained from all participants. Patients were referred for CAPR CE-MRA for assessment of a known or suspected vascular malformation and planning of sclerotherapy. Twelve patient studies (eight female, four male) were performed consecutively from January 2010 to May 2011 and are summarized in Table 1. The average patient age was 33 years, range 14–56 years;

males average age 35.5 years, range 14–48 years; females average age 31.5 years, range 21–56 years. Vascular malformations were imaged in the forearm, hand, thigh, and foot.

MR Data Acquisition

The CAPR sampling pattern, previously described (20), was applied to imaging of peripheral vascular malformations. It is based on a T1-weighted fast gradient echo pulse sequence. CAPR is a time-resolved sampling pattern that uses elliptical centric sampling (27), 2D homodyne processing (28,29), view-sharing (23), and 2D SENSE (19). A central ***k***-space region is defined in the k_Y-k_Z plane and those low spatial frequency views are updated more frequently than the high spatial frequency views. The frame time is the time interval at which a new central ***k***-space region is sampled and a new image is generated. The temporal footprint (20) is the total time over which data used to form a single image are acquired and for this work is approximately four times the frame time.

The acquisition parameters were selected according to the targeted temporal and spatial resolution for each anatomic region. Acquired spatial resolution of 1.0-mm isotropic was targeted in all regions except in the foot where sub-millimeter resolution was targeted for better depiction of small vessels. The targeted frame time varied according to the predicted average flow rate for each region. These were 3.5 s for the hands, approximately 3.5–5.0 s for the forearms and thighs, and 7.0 s for the feet. The field-of-view (FOV) was next specified to cover the targeted region superior/inferior (S/I) and encompass both limbs left/right (L/R) and anterior/posterior (A/P). Then, the matrix size was specified to provide the desired spatial resolution for each region. Finally, the application of the CAPR sampling pattern and 2D SENSE allowed for the acquisition time in each region to be adjusted to approximately match the targeted frame time. The 2D SENSE was applied as $R_Y = 4$, $R_Z = 2$ ($R = 8$) along with 2D homodyne with acceleration $R_{HD} = 1.8$ for a net acceleration of $R_{NET} = 8 \times 1.4 = 14.4$. View-sharing was applied to further reduce the frame time but is not included in the calculation of acceleration. The typical imaging parameters for each region are summarized in Table 2. Throughout the course of the 12 volunteer studies, the matrix and sampling parameters, and thus temporal resolution, were held constant for all cases in a given region. The FOV and slice thickness were modified on a patient-specific basis, leading to a slightly different spatial resolution for each exam.

Imaging Experiments

All studies were performed on a 3 Tesla (T) scanner (Signa GE, v20.0/22.0, Waukesha, WI). All studies except for one were performed bilaterally to allow comparison of the diseased with the contralateral limb. Imaging was done in the coronal orientation for the forearms, hands, and thighs and in the sagittal plane for the feet. The patient was positioned prone, with arms extended above the head, for imaging of the upper extremity and supine for imaging of the lower extremity. For all studies, the coil array was wrapped circumferentially around the patient and the last element clasped to the first. For imaging of the forearms, hands, and feet, a linear, eight-element coil array with A/P elements 10.5×27.1 cm^2 and L/R elements 14.3×27.1 cm^2 was used. For imaging of the thighs, a 10–12 element, modular coil array with elements 14.3×27.1 cm^2 was used with the number of elements adjusted to the patient size. Before the contrast-enhanced CAPR acquisition, SENSE calibration was performed with TR/TE 7.1–8.3/3.4–4.0 ms, flip angle 10°, BW ± 31.25 kHz, FOV identical to that for the CAPR acquisition, and matrix size half that of the CAPR acquisition in Y and Z. The CAPR acquisition used a 3D spoiled gradient echo sequence with TR/TE 5.1–5.8/2.3–2.5 ms, flip angle 30°, BW ± 62.5 kHz and matrix size and nominal FOV as listed in Table 2 for each region. The echo times are relatively long due to the high spatial resolution that is acquired by reading out of a full 320–400 point echo. A gadolinium-based contrast agent Multihance (Bracco, Princeton, NJ, USA) or Ablavar (Lantheus Medical Imaging, N.

Billerica, MA, USA) was administered at 0.1–0.2 mmol/kg or 0.03–0.06 mmol/kg, respectively, at 3 mL/s followed by 20 mL saline at 3 mL/s. Ablavar became available at our institution midway through the study and was used for patients in which postgadolinium images were desired. The contrast dose for each patient is provided in Table 1. The CAPR scan was started before contrast material injection to acquire contrast-free reference frames for subtraction, and the scan was continued for 3–4 min to acquire 36 frames postinjection. After the CAPR time-resolved scan, postcontrast single phase imaging was performed using either a single phase CAPR acquisition or a standard clinical 3D T1-weighted spoiled gradient echo sequence with fat suppression. The single phase CAPR acquisition used the same or finer spatial resolution as the time-resolved acquisition and no view-sharing thereby mimicking an elliptical centric acquisition. The purpose of the late phase image was to allow visualization of slowly filling (e.g., > 5 min postinjection) portions of any lesions with high spatial resolution.

The images were viewed as maximum intensity projections (MIPs) in the acquisition plane and as source images reformatted into arbitrary viewing planes. Additionally, 3D rotational MIPs and time-of-arrival (TOA) maps (30) were generated. The TOA images map the absolute postinjection time of contrast arrival of each voxel to a color scale.

DSA Acquisition

Ten of the 12 patients underwent fluoroscopy-guided sclerotherapy following MRI assessment. Images from the fluoroscopic angiography/venography performed during and after treatment were available for comparison with the CE-MRA time series. With DSA (Siemens, Artis Zee, Muenchen, Germany) 2–4 images per second were acquired with resolution of 2.09 line pairs/mm at the specified field-of-view, 70 ± 5 kVp, and 150 ± 20 mA dependent on thickness. These are average values as acquisition parameters were calculated on a patient specific basis.

Imaging Evaluation

The images were reviewed by a diagnostic radiologist (PMY, two years of experience) and an interventional radiologist (MAM, 25 years of experience), both experienced in MR and CT. The time-resolved CAPR image series was evaluated in 11 categories shown in Table 3 with Categories 1–6 defined for assessing the image quality specific to vascular malformations, Categories 7–8 more general, and Categories 9–10 as related to the subsequent therapy. Each study was scored from 1 to 4 in each category, where 1 generally indicates nondiagnostic and 4 indicates excellent but with specific definitions shown in the table. Correlation with treatment images (Category 10) was performed for the 10 of the total 12 studies for which sclerotherapy treatment was subsequently performed at our institution and for which the angiography images were available for review. Finally, in Category 11 the reviewers were asked to characterize each lesion as high or low flow and whether the extent was focal, multifocal, or diffuse.

The single phase postcontrast images were used for evaluation of Category 6, identification of relationship and involvement of malformation with surrounding tissue, and were assessed for additional information beyond that of the time-resolved image series.

In selected studies, full width at half maximum (FWHM) measurements were made on vessels in the axial slice; i.e., within the phase encoding plane.

Statistical Analysis

The mean ± standard deviation was calculated for each category for each reviewer, and the aggregate scores were determined.

RESULTS

All patients were successfully imaged, and diagnostic image time series were obtained. The results of the radiologic evaluation are shown in Table 4. In lesion characterization (Category 11, not shown in the table), there was 1 case negative for a vascular malformation, and 11 positive with 2 high flow arterial–venous malformations, and 9 low flow venous malformations. Of the 11 positive cases, 2 were focal, 2 were multifocal, and 7 were diffuse. In all cases, the characterization of high versus low flow and extent was corroborated during the subsequent interventional study. There was a total of 22 scores for each category, two reviewers scoring 11 positive cases. In all categories the average score was between 3.25 and 3.91. For all categories except Category 2, at most one of the 22 scores was less than 3 (good–excellent). Category 2, identification of the nidus had a mean score less than 3.0 in two cases, one with very high flow and one with very low flow. The overall quality of the CAPR time series for diagnosis and treatment planning (Category 9) was good to excellent with an average score of 3.58 ± 0.58, with one marginal score (Pt. 4). The correlation with treatment DSA imaging (Category 10) was also excellent with an average score of 3.89 ± 0.46. For all cases of low-flow lesions, both reviewers believed that there was additional diagnostic information provided in the late single phase images.

Figures 1 and 2 show results from Patient 2, a 14-year-old boy with a vascular malformation of the right thigh. Figure 1 shows consecutive coronal (A–C) and targeted (D–F) MIPs from the time-resolved series with a frame time of 4.9 s. Progressive arterial and venous enhancement is depicted with slow filling of the vascular malformation above the right knee (arrow) from the genicular arteries. There is parallel venous drainage with communication back to normal veins. The time-of-arrival map (G) shows peak enhancement of the vascular malformation (red) between the peak arterial (yellow–orange) and venous phases (blue). See Supp. Video SV1, which is available online).

Figure 2 shows slices from the higher spatial resolution ($0.8 \times 0.8 \times 1.1$ mm^3), nonsubtracted late phase image with sharp depiction of the malformation and its location relative to the tissue structures. These images show the draining veins as well as the lack of involvement of the lesion with the bony structures and skin.

Figures 3 and 4 show results from Patient 11, a 46-year-old male with a vascular malformation of the left upper leg. In Figure 3, targeted MIPs from the CAPR time-resolved series are compared with images from conventional angiography at the time of treatment. To illustrate the FWHM analysis, line profiles of vessels located at the mid-thigh with measured FWHM values are shown in Supp. Fig. SF1. See also Supplemental Video SV2.

Figure 4 shows coronal and axial slices from the late single phase CAPR image. These images demonstrate the involvement of the lesion with the sartorius muscle and confirm the extent of the lesion is similar to that depicted in the time-resolved series.

Figure 5 shows results from Patient 7, a 56-year-old female with Park Weber syndrome and a vascular malformation of the left foot. There is rapid contrast passage through the enlarged vessels of the left foot and ankle with dominant blood supply from the anterior tibial artery (A, arrow). The CAPR time series also shows involvement of the malformation with the plantar skin of the foot (D, arrow). See Supp. Video SV3.

Figure 6 shows results from Patient 12, a 34-year-old male with a vascular malformation of the left forearm. Coronal MIPs (A–C) from selected time frames show filling of the normal arterial and venous system as well as abnormal vasculature in the proximal forearm. Single coronal (D–F) and axial (G–I) slices from the corresponding time frames more clearly show the enhancing nidus without the overlaying vasculature. The late phase coronal (J) and axial

(K) images show the full extent of the malformation and involvement with the tissue around the interosseous membrane.

DISCUSSION

In this work, it has been shown that time-resolved CE-MRA using the CAPR technique can provide high temporal and spatial resolution imaging of vascular malformations of the extremities that allows for accurate lesion characterization and treatment planning. In the imaging evaluation Categories 1–3, identification of feeding vessels, early filling nidus and venous outflow all had average scores of 3.41 or higher, indicating good–excellent portrayal of dynamic information of the vascular malformation. Categories 4–6, identification of normal venous structures, malformation extent, and involvement with surrounding tissue had average scores of 3.71–3.91, indicating excellent portrayal of anatomic information. The overall utility of the CAPR time series for diagnosis and treatment planning was scored to be good–excellent with an average score of 3.58, and fidelity was verified by excellent correlation with conventional angiography performed at the time of treatment.

The CAPR sampling parameters were chosen for each imaging region according to the targeted performance for the typical anticipated physiologic arterial flow and were held constant throughout the course of the study. The chosen parameters provided acquired spatial resolution on the order of 1-mm isotropic with 3.5- to 7.0-s frame times. As indicated by the imaging evaluation, the spatial resolution was adequate for depiction of the normal vasculature and the lesion in all cases, and the temporal resolution was fast enough to depict lesion filling and washout in all cases but one.

The late postcontrast single phase image was useful for identification of the full lesion extent, involvement of the malformation with surrounding tissue, and demonstration of venous pooling in slow flow lesions. In some cases, there was improved depiction of very slow flow lesions on the late phase image primarily due to the fact that more time had passed, allowing complete filling of the lesion with contrast-enhanced blood. The involvement of the malformation with the surrounding tissue was assessed using the single phase image, although may also be visualized in the time-resolved series when reconstructed without subtraction of baseline frames. Overall, there was not a significant difference in image quality between late frames from the CAPR time series and the single phase image, as illustrated in Figure 6. Because the enhanced blood signal is quasi-static during acquisition of the late phase image, that single phase image can potentially have higher spatial resolution than those in the dynamic run. Although considerable information can be gathered from the time-resolved series, for slow flow lesions in particular, our evaluation indicates that it is useful to perform late-phase imaging in conjunction.

Prior studies have shown the utility of MRI for defining anatomic extent and categorizing vascular malformations as high or low flow based primarily on the presence or absence of flow voids (6–9) or the contrast rise time (3). Time-resolved CE-MRA used in conjunction with conventional single phase MRI or MRA (4,16–18,31) has been shown to provide a more detailed description and evaluation of malformations. In this work, a highly accelerated (R_{NET} = 14.4) time-resolved CE-MRA acquisition technique was implemented, and a comprehensive evaluation of its performance was done with respect to diagnosis, lesion categorization, and treatment planning. Similar to other studies, we conclude that time-resolved CE-MRA offers information beyond that of single phase MRI/MRA that is useful for diagnosis, treatment planning, and potential reduction of fluoroscopic imaging during intervention. Comparison with DSA allowed verification of the accuracy of the information provided by the time-resolved CE-MRA technique.

Two pitfalls of the time-resolved imaging as performed in this work were inadequate depiction of rapid arterial filling of markedly high flow lesions and inadequate depiction of late filling of markedly slow flow lesions. The depiction of lesion filling and vessel sharpness was marginally degraded in a high flow lesion of the hand (Patient 3) and similarly a high flow lesion of the foot (Patient 7; Fig. 5) due to the rapid flow relative to the frame time and temporal footprint (20). Therefore, in high flow cases such as these it would be advantageous to decrease the frame time and temporal footprint to better portray progressive filling of the lesion. This may be achieved by using coarser spatial resolution, e.g., 1.5-mm isotropic rather than 1-mm isotropic, or possibly in the future by using higher SENSE accelerations than the R = 8 used here. Depiction of delayed filling was marginal in two cases of very slow flow lesions simply because the venous structures were not yet fully enhanced at the end of the CAPR time series. The malformation and venous structures were well-depicted in the late single phase image. These late filling venous structures may be better depicted by the time-resolved series by extending the imaging duration / acquiring more time frames.

There were other limitations to this study. First, there was a limited number of cases, primarily due to the limited number of patients presenting with vascular malformations. Second, the contrast doses used in these patients ranged from a single to a double standard clinical dose. In other work using the CAPR technique (32) contrast doses lower than a single dose (0.1 mmol/kg) were used for time-resolved CAPR imaging and showed high quality, indicating that the use of lower contrast doses is feasible. The contrast doses for this study were chosen to provide good venous opacification in delayed imaging and allow for evaluation of the presence of deep venous thromboses, which would preclude endovascular therapy.

In conclusion, the highly accelerated CAPR time series in conjunction with late-phase imaging has been shown to portray the temporal dynamics and structure of vascular malformations as well as the normal vasculature with high quality and high fidelity, with excellent correlation to DSA. CAPR time-resolved imaging is able to accurately characterize high and low flow lesions, and delayed imaging is important to capture complete filling of very slow flow vascular malformations. Time-resolved CE-MRA may offer improved pretreatment lesion characterization and treatment planning as well as reduce the fluoroscopic imaging to be performed at the time of treatment.

Supplementary Material

Refer to Web version on PubMed Central for supplementary material.

Acknowledgments

We thank Steve Williams for his assistance in the coordination of the patient studies.

Contract grant sponsor: NIH; Contract grant number: EB000212; Contract grant number: HL070620; Contract grant number: RR018898.

REFERENCES

1. Eifert S, Villavicencio JL, Kao TC, Taute BM, Rich NM. Prevalence of deep venous anomalies in congenital vascular malformations of venous predominance. J Vasc Surg. 2000; 31:462–471. [PubMed: 10709058]
2. Hyodoh H, Hori M, Akiba H, Tamakawa M, Hyodoh K, Hareyama M. Peripheral vascular malformations: imaging, treatment approaches, and therapeutic issues. Radiographics. 2005; 25(Suppl 1):S159–S171. [PubMed: 16227489]

3. Ohgiya Y, Hashimoto T, Gokan T, et al. Dynamic MRI for distinguishing high-flow from low-flow peripheral vascular malformations. AJR Am J Roentgenol. 2005; 185:1131–1137. [PubMed: 16247121]
4. Moukaddam H, Pollak J, Haims AH. MRI characteristics and classification of peripheral vascular malformations and tumors. Skeletal Radiol. 2009; 38:535–547. [PubMed: 19020874]
5. Mistretta CA, Crummy AB. Diagnosis of cardiovascular disease by digital subtraction angiography. Science. 1981; 214:761–765. [PubMed: 7292009]
6. Meyer JS, Hoffer FA, Barnes PD, Mulliken JB. Biological classification of soft-tissue vascular anomalies: MR correlation. AJR Am J Roentgenol. 1991; 157:559–564. [PubMed: 1872245]
7. Rak KM, Yakes WF, Ray RL, et al. MR imaging of symptomatic peripheral vascular malformations. AJR Am J Roentgenol. 1992; 159:107–112. [PubMed: 1609682]
8. Dobson MJ, Hartley RW, Ashleigh R, Watson Y, Hawnaur JM. MR angiography and MR imaging of symptomatic vascular malformations. Clin Radiol. 1997; 52:595–602. [PubMed: 9285419]
9. Kim EY, Ahn JM, Yoon HK, et al. Intramuscular vascular malformations of an extremity: findings on MR imaging and pathologic correlation. Skeletal Radiol. 1999; 28:515–521. [PubMed: 10525795]
10. Fayad LM, Hazirolan T, Bluemke D, Mitchell S. Vascular malformations in the extremities: emphasis on MR imaging features that guide treatment options. Skeletal Radiol. 2006; 35:127–137. [PubMed: 16447042]
11. Zhang H, Maki JH, Prince MR. 3D contrast-enhanced MR angiography. J Magn Reson Imaging. 2007; 25:13–25. [PubMed: 17154188]
12. Schneider, G.; Prince, MR.; Meaney, JFM.; Ho, VB., editors. Magnetic resonance angiography: techniques, indications and practical applications. Springer; Milan: 2005.
13. Prince, MR.; Grist, TM.; Debatin, JF., editors. 3D Contrast MR angiography. Springer; Berlin: 2003.
14. van Vaals JJ, Brummer ME, Dixon WT, et al. “Keyhole” method for accelerating imaging of contrast agent uptake. J Magn Reson Imaging. 1993; 3:671–675. [PubMed: 8347963]
15. Korosec FR, Frayne R, Grist TM, Mistretta CA. Time-resolved contrast-enhanced 3D MR angiography. Magn Reson Med. 1996; 36:345–351. [PubMed: 8875403]
16. van Rijswijk CS, van der Linden E, van der Woude HJ, van Baalen JM, Bloem JL. Value of dynamic contrast-enhanced MR imaging in diagnosing and classifying peripheral vascular malformations. AJR Am J Roentgenol. 2002; 178:1181–1187. [PubMed: 11959728]
17. Herborn CU, Goyen M, Lauenstein TC, Debatin JF, Ruehm SG, Kroger K. Comprehensive time-resolved MRI of peripheral vascular malformations. AJR Am J Roentgenol. 2003; 181:729–735. [PubMed: 12933470]
18. Kramer U, Ernemann U, Fenchel M, et al. Pretreatment evaluation of peripheral vascular malformations using low-dose contrast-enhanced time-resolved 3D MR angiography: initial results in 22 patients. AJR Am J Roentgenol. 2011; 196:702–711. [PubMed: 21343517]
19. Weiger M, Pruessmann KP, Boesiger P. 2D SENSE for faster 3D MRI. MAGMA. 2002; 14:10–19. [PubMed: 11796248]
20. Haider CR, Hu HH, Campeau NG, Huston J 3rd, Riederer SJ. 3D high temporal and spatial resolution contrast-enhanced MR angiography of the whole brain. Magn Reson Med. 2008; 60:749–760. [PubMed: 18727101]
21. Lim RP, Shapiro M, Wang EY, et al. 3D time-resolved MR angiography (MRA) of the carotid arteries with time-resolved imaging with stochastic trajectories: comparison with 3D contrast-enhanced bolus-chase MRA and 3D time-of-flight MRA. AJNR Am J Neuroradiol. 2008; 29:1847–1854. [PubMed: 18768727]
22. Fink C, Ley S, Kroeker R, Requardt M, Kauczor HU, Bock M. Time-resolved contrast-enhanced three-dimensional magnetic resonance angiography of the chest: combination of parallel imaging with view sharing (TREAT). Invest Radiol. 2005; 40:40–48. [PubMed: 15597019]
23. Riederer SJ, Tasciyan T, Farzaneh F, Lee JN, Wright RC, Herfkens RJ. MR fluoroscopy: technical feasibility. Magn Reson Med. 1988; 8:1–15. [PubMed: 3173063]

24. Haider CR, Glockner JF, Stanson AW, Riederer SJ. Peripheral vasculature: high-temporal- and high-spatial-resolution three-dimensional contrast-enhanced MR angiography. Radiology. 2009; 253:831–843. [PubMed: 19789238]
25. Mostardi PM, Haider CR, Glockner JF, Young PM, Riederer SJ. High spatial and temporal resolution imaging of the arterial vasculature of the lower extremity with contrast enhanced MR angiography. Clin Anat. 2011; 24:478–488. [PubMed: 21509813]
26. Haider, CR.; Glockner, JF.; Stanson, AW.; Riederer, SJ. High temporal and spatial resolution time-resolved 3D CE-MRA of the hands and feet. Proceedings of the Joint Annual Meeting of ISMRMESMRMB; Honolulu. 2009.
27. Wilman AH, Riederer SJ. Performance of an elliptical centric view order for signal enhancement and motion artifact suppression in breath-hold three-dimensional gradient echo imaging. Magn Reson Med. 1997; 38:793–802. [PubMed: 9358454]
28. Noll DC, Nishimura DG, Macovski A. Homodyne detection in magnetic resonance imaging. IEEE Trans Med Imaging. 1991; 10:154–163. [PubMed: 18222812]
29. Madhuranthakam AJ, Hu HH, Barger AV, et al. Undersampled elliptical centric view-order for improved spatial resolution in contrast-enhanced MR angiography. Magn Reson Med. 2006; 55:50–58. [PubMed: 16315207]
30. Riederer SJ, Haider CR, Borisch EA. Time-of-arrival mapping at three-dimensional time-resolved contrast-enhanced MR angiography. Radiology. 2009; 253:532–542. [PubMed: 19789236]
31. Flors L, Leiva-Salinas C, Maged IM, et al. MR imaging of soft-tissue vascular malformations: diagnosis, classification, and therapy follow-up. Radiographics. 2011; 31:1321–1340. discussion 1340–1321. [PubMed: 21918047]
32. Mostardi PM, Glockner JF, Young PM, Riederer SJ. Contrast-enhanced MR angiography of the abdomen with highly accelerated acquisition techniques. Radiology. 2011; 261:587–597. [PubMed: 21900616]

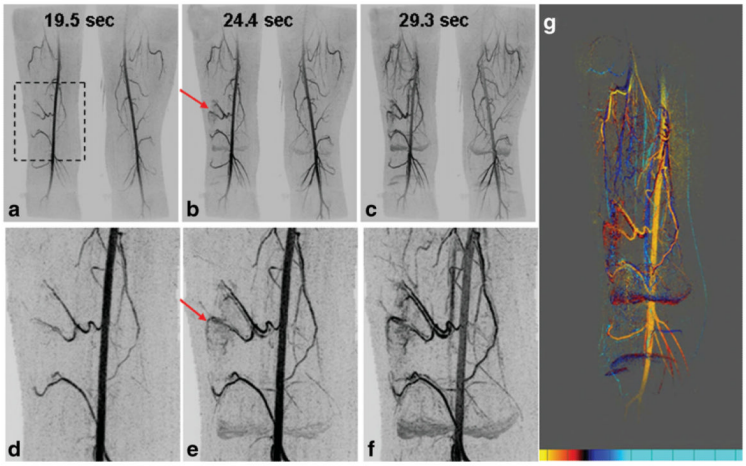

Figure 1.

Results from a time-resolved study of Patient 2, a 14-year-old male with a vascular malformation in his right vastus intermedius referred for CAPR imaging for planning of MR-guided sclerotherapy. Consecutive coronal (**a–c**) and targeted (**d–f**) MIPs from the sub-region identified in (a) show progressive filling of the malformation (arrow) with sharp anatomic detail. The time-of-arrival map (**g**) shows arterial feeding vessels (yellow), late arterial/early venous phase (red), and venous drainage (blue).

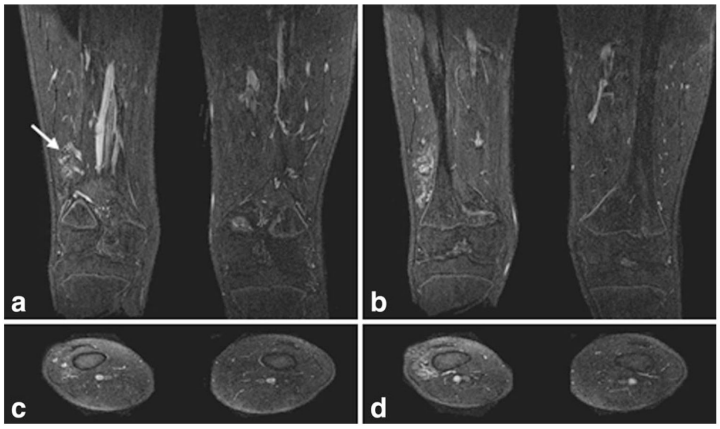

Figure 2.

Single 1.1-mm-thick coronal and axial slices from the high spatial resolution, nonsubtracted late phase image from Patient 2. Single coronal slices (**a,b**, anterior to posterior) and axial slices (**c,d**, superior to inferior) show the fine detail of the vascular malformation located in the right vastus intermedius with no bony involvement. Enlarged draining veins (arrow) are shown in (a). The 3D volume imaged in this late phase scan is the same as that for the CAPR time series.

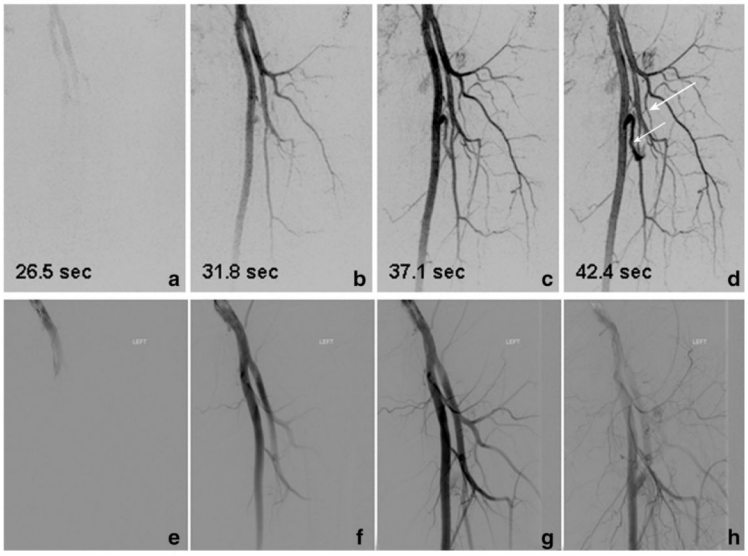

Figure 3.

Results from a time-resolved study of Patient 11, a 46-year-old male with a vascular malformation of the left upper leg. Consecutive targeted MIPs (**a–d**) show feeding vessels to the nidus (short arrow). The time series portrays feeding of the lesion by means of the circumflex femoral artery (long arrow). Every other image from the from fluoroscopic angiography series (**e–h**) performed at the time of treatment that show excellent correlation with the CAPR time series.

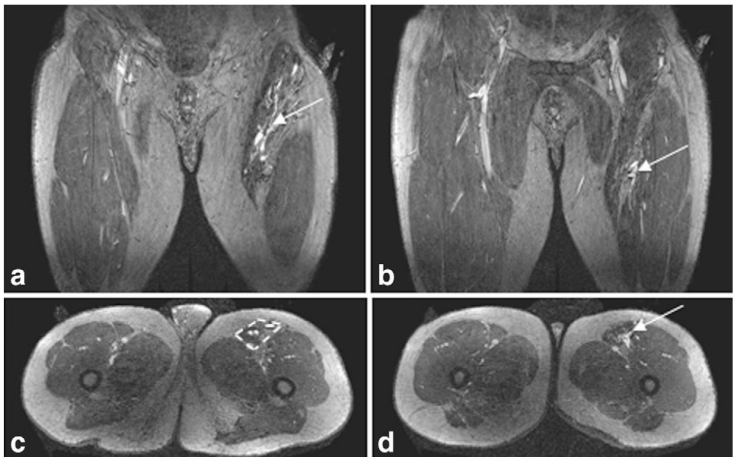

Figure 4.
Coronal (**a,b**) and axial (**c,d**) slices from the late phase imaging in Patient 11 shows that the lesion is restricted to the sartorius muscle, with the muscle compartment outlined (c, dashed yellow box). (a) and (c) depict the more proximal portion of the lesion and (b) and (d) the more distal part of the lesion.

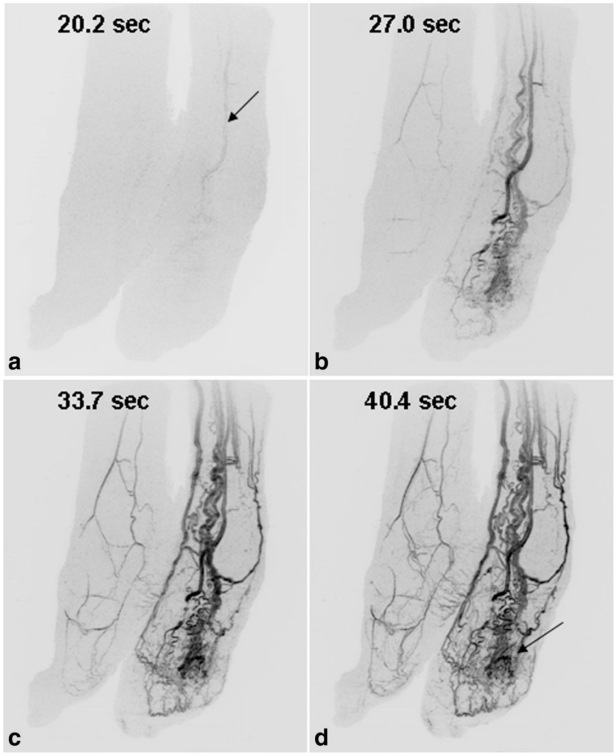

Figure 5.
Results from Patient 7, a 56-year-old woman with a vascular malformation of the left foot (**a–d**). Oblique MIPs of both feet show rapid contrast passage through the enlarged vessels of the left foot compared with the right foot. Dominant supply to the malformation is from the anterior tibial artery (arrow, A). The time series also shows involvement of the malformation with the plantar skin of the foot (D, arrow).

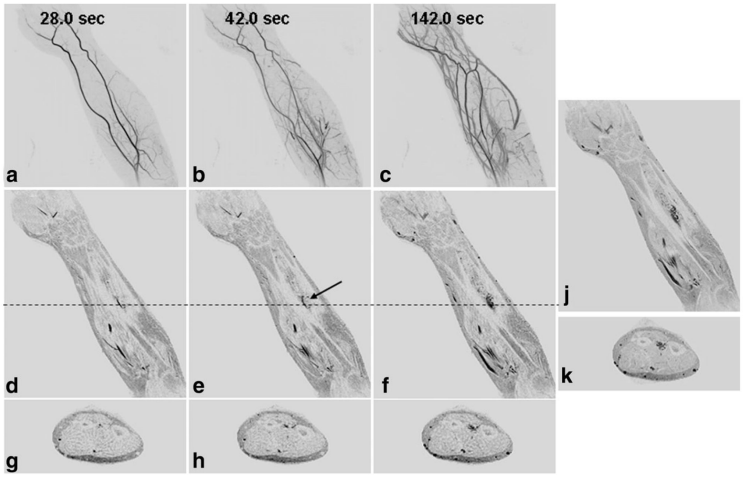

Figure 6.

Results from the CAPR time-resolved series and late phase imaging from Patient 12, a 34-year-old male with a vascular malformation of the left forearm. Coronal MIPs (**a–c**), coronal slices (**d–f**), and axial slices (**g–i**) from the time-resolved series with a 3.5-s frame time show progressive arterial and venous filling with late enhancement of the malformation. Due to the enhancement of the superficial veins, it is difficult to identify the enhancement of the malformation in the MIP images. The malformation is more clearly seen in the slices. Coronal and axial slices from the last time-resolved image (f,i) show similar depiction of the malformation as the late single phase image (**j,k**).

Table 1

Summary of CAPR AVM Patients

Pt	Region	M/F	Age	Weight (kg)	Agent	Contrast (ml)	(mmol/kg)	Flow
1	Forearm	F	21	50.0	Multihance	20.0	0.20	low
2	Thigh	M	14	49.9	Multihance	16.0	0.16	low
3	Hand	F	27	81.6	Multihance	20.0	0.12	high
4	Feet	M	48	97.5	Multihance	20.0	0.10	low
5	Thigh	F	26	78.9	Multihance	16.0	0.10	low
6	Thigh	F	34	99.8	Multihance	40.0	0.20	low
7	Feet	F	56	90.3	Ablavar	20.0	0.06	high
8	Thigh	F	39	63.5	Ablavar	14.0	0.06	low
9	Thigh	F	28	90.7	Multihance	32.0	0.18	low
10	Hand	F	21	59.0	Multihance	20.0	0.17	
11	Thigh	M	46	89.4	Ablavar	15.5	0.04	low
12	Forearm	M	34	112.0	Ablavar	27.0	0.06	low

Table 2

Summary of acquisition parameters for CAPR AVM studies

Anatomy	Matrix	FOV (cm)	Spatial Resolution (mm^3)	Frame Time (sec)	Temporal Ftpt
Forearm	400 × 360 × 108	40.0 × 36.0 × 10.8	1.0 × 1.0 × 1.0	4.6	16.1
Hand	320 × 256 × 108	32.0 × 25.6 × 10.8	1.0 × 1.0 × 1.0	3.5	12.6
Thigh	400 × 400 × 132	40.0–48.0 × 40.0–48.0 × 13.2–26.4	1.0–1.2 × 1.0–1.2 × 1.0–2.0	5.6	20.1
Foot	400 × 320 × 220	30.0 × 24.0 × 24.2	0.75 × 0.75 × 1.1	7.0	25.3

Table 3

Evaluation criteria for CAPR time-resolved CE-MRA of peripheral vascular malformations

Category 1: Identification of feeding vessel(s)
1 Not adequately depicted
2 Marginal
3 Good
4 Excellent
Category 2: Identification of early filling nidus
1 Not adequately depicted
2 Marginal
3 Good
4 Excellent
Category 3: Ability to adequately characterize venous outflow
1 Not adequately depicted
2 Marginal
3 Good
4 Excellent
Category 4: Ability to identify normal venous structures
1 Not adequately depicted
2 Marginal
3 Good
4 Excellent
Category 5: Demonstration of malformation extent (focal, multifocal, diffuse)
1 Not adequately depicted
2 Marginal
3 Good
4 Excellent
Category 6: Identification of relationship and involvement of malformation with tissue
1 Not adequately depicted
2 Marginal
3 Good
4 Excellent
Category 7: Vessel sharpness
1 Poor spatial resolution, little or no definition of structure
2 Slight blurring of vessels, likely to impair diagnosis
3 Good visualization of vessel margins, adequate for diagnosis
4 Excellent visualization of vessel margins
Category 8: Presence of artifact (motion, undersampling, aliasing)
1 Severe, nondiagnostic
2 Substantial artifact, mildly/moderately impairs diagnosis

	3 Some artifact present, does not impair diagnosis
	4 No artifact
Category 9: Overall quality for diagnosis and treatment planning	
	1 Nondiagnostic
	2 Marginal
	3 Good
	4 Excellent
Category 10: Correlation of filling pattern and vessel morphology with treatment images	
	1 Poor
	2 Marginal
	3 Good
	4 Excellent
Category 11: Characterization of malformation pattern (circle one)	
	Flow: high or low
	Extent: focal or diffuse
Additional information provided by late single phase imaging	
	Yes No

Table 4

Aggregate results (mean ± std) from radiologic evaluation n = 12 for all categories except n = 10 for Category 10

Category 1: Identification of feeding vessel(s)	3.55 ± 0.67
Category 2: Identification of filling nidus	3.41 ± 0.80
Category 3: Characterization of venous outflow	3.68 ± 0.57
Category 4: Identification of normal venous structures	3.67 ± 0.56
Category 5: Demonstration of malformation extent	3.83 ± 0.64
Category 6: Identification of tissue involvement	3.91 ± 0.29
Category 7: Vessel sharpness	3.71 ± 0.46
Category 8: Presence of artifact	3.25 ± 0.53
Category 9: Quality for diagnosis and treatment planning	3.58 ± 0.58
Category 10: Correlation with treatment images	3.89 ± 0.46